Article

Orbital Fulde–Ferrell–Larkin–Ovchinnikov state in an Ising superconductor

Puhua Wan[1], Oleksandr Zheliuk[1,2], Noah F. Q. Yuan[3], Xiaoli Peng[1], Le Zhang[1], Minpeng Liang[1], Uli Zeitler[2], Steffen Wiedmann[2], Nigel E. Hussey[2,4], Thomas T. M. Palstra[5] & Jianting Ye[1✉]

In superconductors possessing both time and inversion symmetries, the Zeeman effect of an external magnetic field can break the time-reversal symmetry, forming a conventional Fulde–Ferrell–Larkin–Ovchinnikov (FFLO) state characterized by Cooper pairings with finite momentum[1,2]. In superconductors lacking (local) inversion symmetry, the Zeeman effect may still act as the underlying mechanism of FFLO states by interacting with spin–orbit coupling (SOC). Specifically, the interplay between the Zeeman effect and Rashba SOC can lead to the formation of more accessible Rashba FFLO states that cover broader regions in the phase diagram[3–5]. However, when the Zeeman effect is suppressed because of spin locking in the presence of Ising-type SOC, the conventional FFLO scenarios are no longer effective. Instead, an unconventional FFLO state is formed by coupling the orbital effect of magnetic fields with SOC, providing an alternative mechanism in superconductors with broken inversion symmetries[6–8]. Here we report the discovery of such an orbital FFLO state in the multilayer Ising superconductor 2H-NbSe$_2$. Transport measurements show that the translational and rotational symmetries are broken in the orbital FFLO state, providing the hallmark signatures of finite-momentum Cooper pairings. We establish the entire orbital FFLO phase diagram, consisting of a normal metal, a uniform Ising superconducting phase and a six-fold orbital FFLO state. This study highlights an alternative route to achieving finite-momentum superconductivity and provides a universal mechanism to preparing orbital FFLO states in similar materials with broken inversion symmetries.

In a conventional superconductor, when spatial inversion and time-reversal symmetries are respected, electrons form Cooper pairs with opposite momenta and spins as described by the Bardeen–Cooper–Schrieffer (BCS) theory (Fig. 1a). Breaking either of the two symmetries can lead to unconventional Cooper pairing with non-trivial spin or momentum configurations. The absence of spatial inversion symmetry, for example, can result in a Rashba- or Ising-type SOC, which enhances the paramagnetic limiting field beyond the Pauli limit B_P along particular directions[9–11]. Breaking time-reversal symmetry by the Zeeman effect of an external magnetic field, on the other hand, can lead to the FFLO state, in which Cooper pairs acquire a non-zero momentum q (refs. 1,2) (Fig. 1b). This conventional FFLO state can be stabilized in a clean superconductor[12,13] through a first-order phase transition from the BCS phase at low temperatures, namely, $T < T_{FFLO} \cong 0.56T_{c0}$ and high fields, namely, $B > B_{FFLO} \cong 0.75\Delta_0/\mu_m$. Here T_{c0} is the critical temperature at the zero magnetic (B) field, Δ_0 is the pairing potential at zero field and zero temperature and μ_m is the electron magnetic moment[14,15].

Simultaneously breaking the inversion and time-reversal symmetries is predicted to lead to an even richer manifold of finite-momentum pairing states beyond conventional FFLO[4–7,16]. In a Rashba-type

superconductor, SOC polarizes the in-plane spin configuration. The Zeeman effect from a parallel external field can then deform the Fermi surface and stabilize finite-momentum pairing (Fig. 1c). In this way, Rashba SOC can extend the FFLO state to higher temperatures and lower magnetic-field strengths relative to the conventional FFLO limits defined above[4,5,16].

Despite the symmetry differences, the Zeeman effect configures both conventional and Rashba FFLOs. Considering that the orbital and Zeeman effects are simultaneously exerted by an external magnetic field, favouring the Zeeman effect requires suppression of the orbital effect. Crucially, the Cooper pairs should not be disrupted by orbital depairing before the Zeeman effect has driven them through an FFLO transition. This explains why FFLO states have been widely reported in heavy-fermion superconductors[17,18] or low-dimensional superconductors[19–23] in which the orbital effect is weakened.

Contrary to conventional wisdom, we show here that the interlayer orbital effect from an external B field can assist FFLO formation in an Ising superconductor in which the Zeeman effect is suppressed. In transition metal dichalcogenides, local symmetry breaking in individual layers induces strong Ising SOC, alternately locking spins at the K/K′

[1]Device Physics of Complex Materials, Zernike Institute for Advanced Materials, University of Groningen, Groningen, The Netherlands. [2]High Field Magnet Laboratory (HFML-EMFL), Radboud University, Nijmegen, The Netherlands. [3]School of Science, Harbin Institute of Technology, Shenzhen, China. [4]H. H. Wills Physics Laboratory, University of Bristol, Bristol, UK. [5]Nano Electronic Materials, University of Twente, Enschede, The Netherlands. ✉e-mail: j.ye@rug.nl
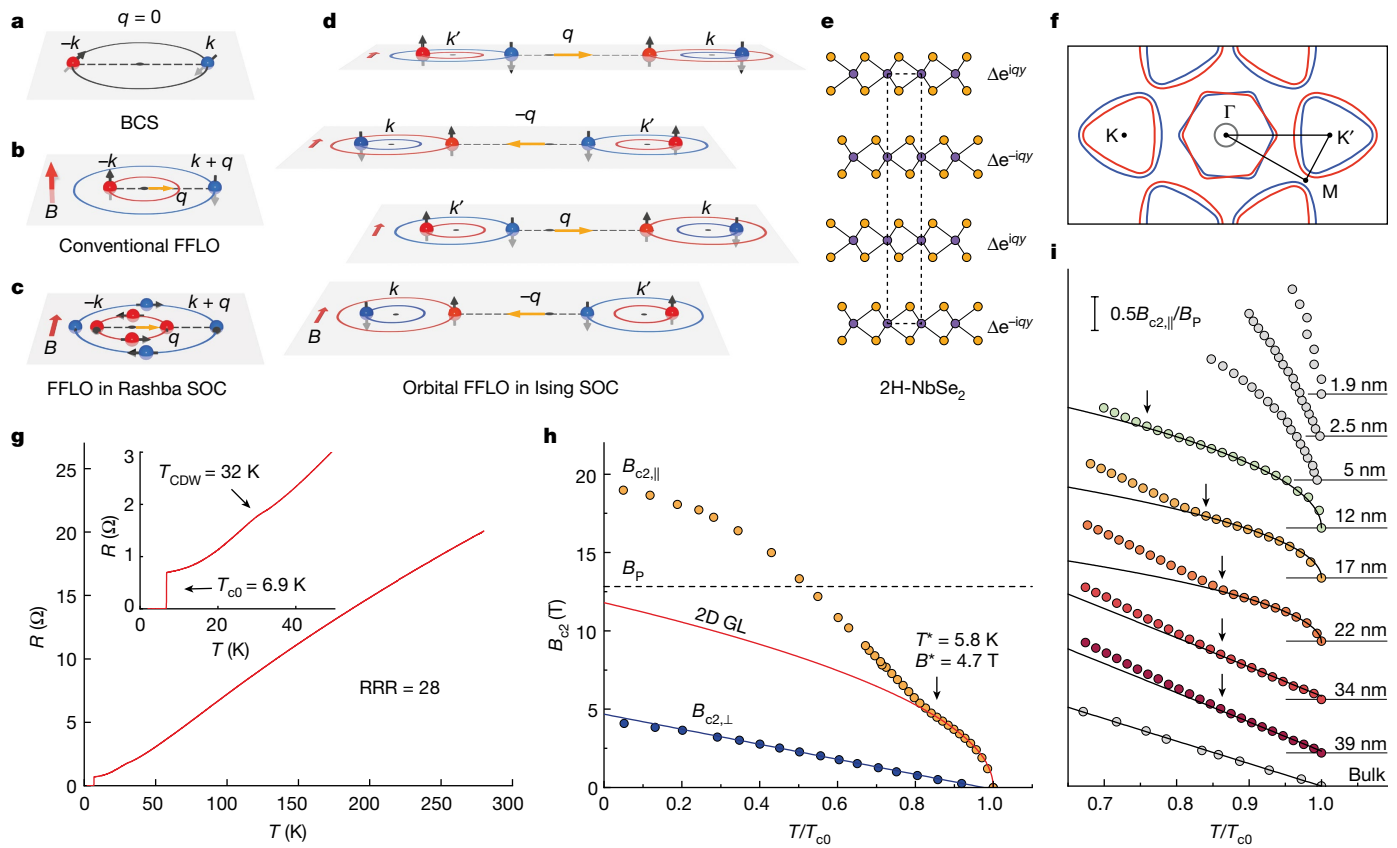
a $q = 0$

$-k$ k

BCS

b

B $-k$ $k + q$ q

Conventional FFLO

c

B $-k$ $k + q$ q

FFLO in Rashba SOC

d

k' q k

k $-q$ k'

k' q k

B k $-q$ k'

Orbital FFLO in Ising SOC

e

Δe^{iqy}

Δe^{-iqy}

Δe^{iqy}

Δe^{-iqy}

2H-NbSe$_2$

f

K Γ K'

M

g

$T_{CDW} = 32$ K

$T_{c0} = 6.9$ K

RRR = 28

h

$B_{c2,\parallel}$

B_P

2D GL

$T^* = 5.8$ K
$B^* = 4.7$ T

$B_{c2,\perp}$

i

$0.5B_{c2,\parallel}/B_P$

1.9 nm

2.5 nm

5 nm

12 nm

17 nm

22 nm

34 nm

39 nm

Bulk

Fig. 1 | Superconductivity and possible pairing states in NbSe$_2$ multilayers. **a**, BCS pairing with zero momentum. **b**, Conventional FFLO pairing with finite momentum q. The Zeeman effect of the external B field induces spin imbalance. **c**, A representative of finite-momentum pairings in Rashba superconductors[4,16]. The Rashba SOC locks spin in the in-plane direction. The finite-momentum pairing is then induced by coupling between the Rashba SOC and the Zeeman effect of parallel fields. The sphere with an arrow represents an electron and spin in **b** and **c**. **d**, Finite-momentum pairing in a 2H-stacked multilayer Ising superconductor. A strong Ising SOC locks spin to the out-of-plane directions and suppresses the Zeeman effect of an in-plane field. The orbital effect from the parallel B field shifts the centre of the Fermi pockets away from the K/K' point of the Brillouin zone. Pairing the k and k' electrons in the shifted Fermi pockets of the lth layer satisfies $k - k' = (-)^l \mathbf{q}$. **e**, Spatial modulation of the superconducting order parameter in the orbital FFLO state of 2H-NbSe$_2$.

f, Illustration of the Fermi surface of a NbSe$_2$ monolayer. The red and blue colours denote two spin states polarized up and down. The superconducting gap opens at the Nb-derived K/K' (trigonal) and Γ (hexagonal) pockets. **g**, Temperature dependence of the resistance of a 17-nm-thick flake showing large RRR = 28. The enlarged low-temperature part (inset) shows the CDW transition at $T_{CDW} = 32$ K and superconducting transition at $T_c = 6.9$ K. **h**, Temperature dependencies of the upper critical field for fields applied parallel (red; $B_{c2,\parallel}$) and perpendicular (blue; $B_{c2,\perp}$) to the 2D crystal plane. An upturn is observed at (T^*, B^*). The blue line is a fit using the 3D Ginzburg–Landau model for the upper critical field. The red line is a fit using the 2D Ginzburg–Landau model at $T > T^*$. **i**, Thickness dependencies on $B_{c2,\perp}/B_P$ as a function of T/T_{c0}. The abrupt upturn is observed in the intermediate-thickness range between 10 and 40 nm. The error bars are smaller than the symbol size.

valley of the Brillouin zone. This strong locking effect suppresses the change in spin configuration of Cooper pairs under a parallel external field[10,11], prohibiting the Zeeman effect from driving the system into conventional FFLO states. This broken local symmetry is globally restored in a multilayer Ising superconductor with 2H stacking. As shown in Fig. 1d, a weak interlayer orbital effect can shift the energy bands and stabilize a finite-momentum pairing with opposite momentum q in adjacent layers[6]. Furthermore, this orbital FFLO state has a real-space oscillating phase in the order parameter (Fig. 1e). Compared with conventional FFLO, the new mechanism can realize the FFLO state in field strengths substantially smaller than B_P and at a temperature closer to T_{c0}, thereby covering a much broader proportion of the phase diagram[6,7]. We noticed that an orbital-field-driven Fulde–Ferrell pairing state in a moiré bilayer transition metal dichalcogenide was studied in a recent theoretical work (V. K. T. Law, personal communication).

Here we report the experimental realization of the orbital FFLO state in a multilayer Ising superconductor (2H-NbSe$_2$). The finite-momentum pairing emerges below a tri-critical point at $T^* = 0.84T_{c0}$ and $B^* = 0.36B_P$ in which the orbital effect of the parallel B field couples superconducting

layers through the Josephson interaction. Translational and rotational symmetries are broken across the tri-critical point, as revealed by transitions in the vortex dynamics and in-plane anisotropy, respectively. These broken symmetries provide the hallmark signatures of finite-momentum Cooper pairs induced by the formation of an orbital FFLO state. After the characteristic symmetry behaviour, we map the boundary of the first-order transition and establish the full phase diagram of the states.

Phase transition to an orbital FFLO state

We prepare multilayer NbSe$_2$ flakes covered by hexagonal boron nitride flakes to ensure high-quality transport with a large residual resistivity ratio (RRR), which is on par with bulk single crystals[24]. As shown in Fig. 1g, the RRR, defined as $R(280 \text{ K})/R(8 \text{ K})$, reaches 28 for a 17-nm-thick flake. A sharp superconducting transition is observed at $T_{c0} = 6.9$ K, after the charge density wave (CDW) transition at $T_{CDW} \approx 32$ K. The angular dependencies of magnetoresistance are measured by orienting the external B field to the two-dimensional (2D) crystal planes. Figure 1h
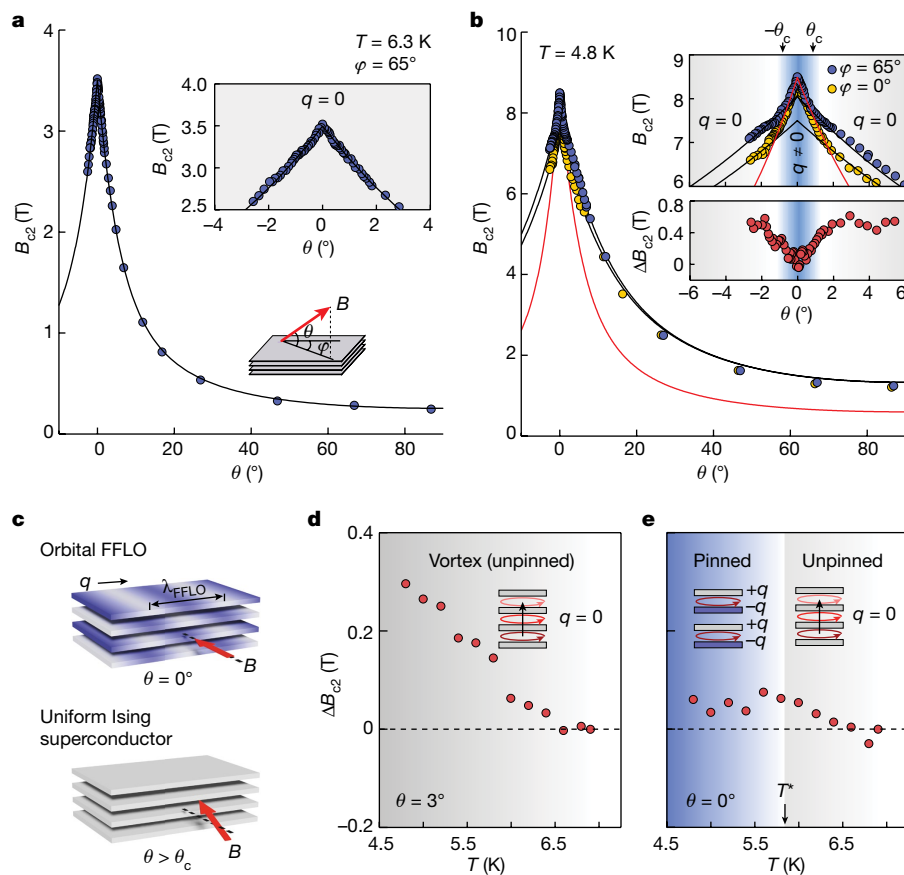
Fig. 2 | Upper critical fields and vortex dynamics in the orbital FFLO state. The direction of the applied current **I** in the 17-nm flake is kept along the direction for the measurements shown in Fig. 3c–i. **a,b**, The B_{c2} value as a function of polar angle θ measured at $T = 6.3$ K $> T^*$ (**a**) and $T = 4.8$ K $< T^*$ (**b**). The insets are enlarged views near $\theta = 0°$. At $T = 6.3$ K, B_{c2} shows one cusp shape that can be fitted by a single 2D Tinkham component for the whole θ range. At $T = 4.8$ K, the B_{c2} fit requires an extra 2D Tinkham component with a larger B_{c2} value for $|\theta| < \theta_c = 1°$. The increase in B_{c2} at $|\theta| < \theta_c$ indicates the formation of the orbital FFLO phase. The bottom inset in **b** shows $\Delta B_{c2} = B_{c2}(\varphi = 65°) − B_{c2}(\varphi = 0°)$ as a function of θ. As shown in Fig. 3c–i, $\varphi = 65°$ and $0°$ are the two representative angles at which the Lorentz forces are weak and strong, respectively. In the uniform phase at $|\theta| > \theta_c$, compared with the weak Lorentz force at $\varphi = 65°$, the stronger Lorentz force at $\varphi = 0°$ suppresses B_{c2} by activating the interlayer vortex motion, thereby causing $\Delta B_{c2} > 0$. The influence of the Lorentz force on B_{c2} disappears at $|\theta| < \theta_c$ for which the vortex motion is pinned after forming the FFLO state. **c**, Schematic for destroying the orbital FFLO state when tilting the B field to $|\theta| > \theta_c$. The stripes (top) illustrate the real-space phase variation in the order parameters, showing wavelength $\lambda_{FFLO} = 2\pi/q$. Here q in the lth layer is $\mathbf{q}_l \propto (−)^l(\mathbf{B} \times \mathbf{z})$, which is perpendicular to the $\mathbf{B}$ field. **d,e**, The influence of Lorentz force, indicated by ΔB_{c2}, is plotted as a function of temperature, showing the temperature dependence of the vortex pinning effect for the uniform phase at $\theta = 3°$ (**d**) and the orbital FFLO phase at $\theta = 0°$ (**e**). For $\theta = 3°$, the ΔB_{c2} value gradually grows with decreasing temperature below T^* due to the unpinned vortex motion in the uniform phase. However, for $\theta = 0°$, $\Delta B_{c2} \approx 0$ at $T < T^*$, indicating vortex pinning in the orbital FFLO phase.

shows the upper critical fields, namely, $B_{c2,\perp}$ and $B_{c2,\parallel}$, measured down to 0.3 K. Here B_{c2} is determined as the B field for which $R = 0.5R_N$ (Supplementary Fig. 6). From $B_{c2,\perp}(T)$, we estimate the Pippard coherence length $\xi_0 = 11.2$ nm, which is smaller than the estimated mean free path $l_m \approx 30$ nm in our device, and comparable with that reported in high-quality bulk crystals ($l_m = 27$ nm)[25]. Satisfying $l_m > \xi_0$ locates our superconducting states within the clean regime (Supplementary Information section 1).

In the $B_\parallel$ configuration, $B_{c2,\parallel}(T)$ follows a square-root dependence near T_{c0}, consistent with a 2D Ginzburg–Landau description (Fig. 1h) for the upper critical field, that is, $B_{c2,\parallel} = \frac{\sqrt{3}\phi_0}{\pi\xi_\parallel(0)d}\left(1 − \frac{T}{T_{c0}}\right)^{\frac{1}{2}}$, of a 2D superconductor with thickness d (Extended Data Fig. 1). With decreasing T, $B_{c2,\parallel}(T)$ shows a conspicuous upturn absent in either bulk[26] or few-layer thin flakes[11,27]. Similar upturns can also be observed in other high-quality flakes with intermediate thicknesses of tens of nanometres (Fig. 1i).

With the increase in NbSe$_2$ thickness from the monolayer to the bulk, the extrapolated $B_{c2,\parallel}(0$ K$)$ varies gradually from $>6B_P$ to $\sim B_P$ (refs. 11,26,27). This notable decrease in $B_{c2,\parallel}$ is caused by a gradual increase in interlayer Josephson coupling J as the flakes get thicker:

from $J = 0$ in a monolayer to its maximum in the bulk[27]. In thicker flakes, the increase in J substantially weakens the Ising protection in individual layers[28]. At a thickness of 17 nm (Fig. 1h), $B_{c2,\parallel} = 1.5B_P$ is found to be intermediate between $B_{c2,\parallel}$ values reported in the bulk[26] and bilayers[27], indicating a reduced J compared with the bulk crystals. It is worth noting that the upturn in $B_{c2,\parallel}$ is absent in bilayer NbSe$_2$ (ref. 27) and our 12-nm sample with increased disorder (Extended Data Fig. 1), confirming that high-quality transport is a crucial prerequisite for realizing the orbital FFLO state.

The upturn at $T^* = 5.8$ K ($0.84T_{c0}$) and $B^* = 4.7$ T ($0.36B_P$) (Fig. 1h) is consistent with the theoretical prediction for the tri-critical point of the orbital FFLO state[6,7]. Note that T^* is considerably higher than the $0.56T_{c0}$ value required for the conventional FFLO state[14,15]. Moreover, B^* is much smaller than B_P as the Zeeman effect, required for forming a conventional FFLO state, is replaced by a new mechanism based on interlayer orbital coupling when strong orbital depairing is absent in $B_\parallel$. Guided by T^* and B^*, we then examine several hallmark signatures related to spatial symmetry, including vortex dynamics[29,30] and anisotropy transition[31,32], to distinguish the FFLO state from the uniform phase.
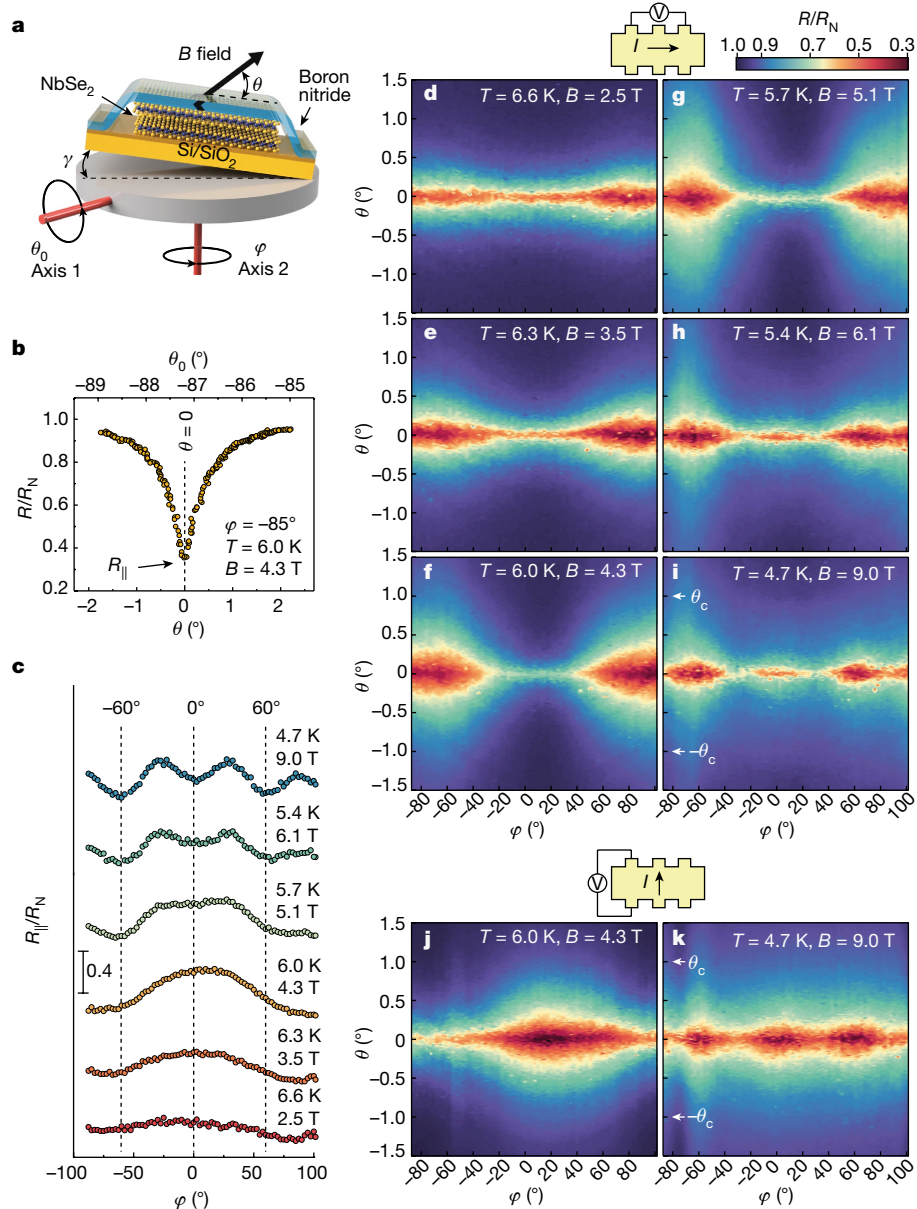
Fig. 3 | Six-fold anisotropy in the orbital FFLO state (measured in the 17-nm flake). a, Schematic of a two-axis rotation stage with the device mounted in a small canting angle γ that varies in each device installation. **b**, Polar angle θ dependence of magnetoresistance determines the $\theta = 0°$ orientation in which the measured R value is defined as $R_{\parallel}$. **c**, Magnetoresistance $R_{\parallel}(\varphi)$ in parallel B fields. **d–i**, Mapping of $R(\varphi, \theta)$ after the subtraction of canting angle $\gamma = 0.78°$, showing a two-fold to six-fold anisotropy transition across the tri-critical point (T^*, B^*). The six-fold anisotropy can be observed only at $|\theta| < \theta_c$, which is consistent with the critical angle observed in Fig. 2b. **j–k**, Mapping of $R(\varphi, \theta)$ after the rotation of **I** to the orthogonal direction. The two-fold anisotropy shifts along with the direction of **I**, indicating the extrinsic origin of the two-fold anisotropy. By contrast, the six-fold anisotropy is independent of the **I** directions, which is consistent with the intrinsic anisotropy of the orbital FFLO phase.

Translational symmetry breaking in the FFLO state

When the FFLO state is established by interlayer orbital coupling under $B_{\parallel}$ (ref. 33), tilting B fields away from the parallel direction can cause a transition from the FFLO state to the uniform phase, providing a preliminary identification of the FFLO state. Figure 2a,b shows the distinctive polar angle (θ) dependencies of B_{c2} across the critical point (T^*, B^*). At $T = 6.3$ K, above T^*, $B_{c2}(\theta)$ exhibits a single cusp centred at $\theta = 0°$, which agrees with a 2D Tinkham fit for a uniform superconductor (Fig. 2a). At $T = 4.8$ K, below T^*, $B_{c2}(\theta)$ shows a sharper enhancement within a critical angle $|\theta_c| \approx 1°$ (Fig. 2b). Tentatively, the dependence of $B_{c2}(\theta)$ below θ_c can be described by an additional Tinkham fit with a larger $B_{c2,\parallel}$. When orbital depairing is suppressed at $|\theta| < \theta_c$, the FFLO state is favourable

(Fig. 2c) as it lowers the free energy compared with the uniform phase. Consequently, the FFLO transition across T^* can cause an anomalous enhancement of B_{c2} (refs. 20,22,34).

Stabilizing the orbital FFLO state breaks the uniform order parameter of a multilayer NbSe$_2$ by adding alternating phase modulation in the out-of-plane direction (Fig. 1e), which is predicted to leave distinctive features in the vortex dynamics[29,31]. Owing to the local translational symmetry breaking of the superconducting order parameter, the interlayer vortex motion is pinned in the FFLO state. To probe the vortex dynamics in the orbital FFLO state, we measure $B_{c2,\parallel}$ as a function of the Lorentz force as $\mathbf{F} = \mathbf{I} \times \mathbf{B}$, which points towards the out-of-plane direction. The associated $\mathbf{F}$ drives interlayer vortex motion in the uniform phase, reducing B_{c2} through dissipation[35]. At the phase boundary between
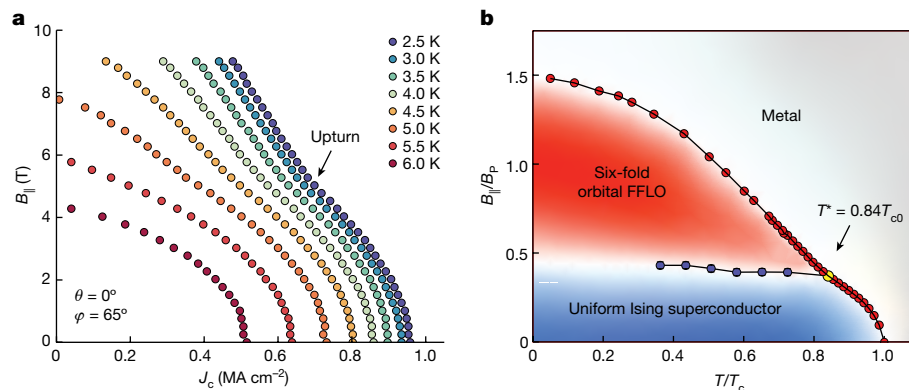
Fig. 4 | Phase diagram of the orbital FFLO state under parallel magnetic fields. a, Magnetic-field dependence of critical current density J_c at different temperatures. The upturns observed at lower temperatures broaden with increasing temperatures. At $T \geq 6$ K, the upturn vanishes. **b**, Phase diagram of the orbital FFLO state. The metal–superconductor phase boundary (red and yellow dots) is determined by measuring the temperature dependence of $B_{c2,\parallel}$ (Fig. 1h). The superconducting phase is divided into uniform Ising superconductivity and the metal and orbital FFLO states, which is of the second order, thermal fluctuations destroy the long-range coherence, forming a coexisting metal–orbital FFLO state. The vortex pinning can 'lock' B_{c2} against **F** as a fingerprint of the oscillating order parameter. As shown in Fig. 2b (top inset), the vortex pinning effect manifests itself as a change in critical field strength $\Delta B_{c2} = B_{c2}(\varphi = 65°) - B_{c2}(\varphi = 0°)$ for which φ is the azimuthal angle within the conducting plane (Extended Data Fig. 4). Here **F** is weaker at $\varphi = 65°$ compared with $\varphi = 0°$ (Fig. 3c–f). As shown in the Fig. 2b (bottom inset), $\Delta B_{c2} \approx 0$ T at $\theta = 0°$ and quickly reaches almost 0.4 T for $|\theta| > \theta_c$. Within a small tilt angle θ, **F** can be regarded as a constant. Therefore, the result of $\Delta B_{c2}(\theta) = 0$ indicates a strong vortex pinning effect, surpassing the dominance of the Lorentz force due to the oscillating phases in the FFLO state. Such a pinning effect is absent in the uniform superconducting phase when $|\theta| > \theta_c$, as indicated by a finite ΔB_{c2}.

Figure 2d,e shows $\Delta B_{c2}(T)$ along the normal–superconducting phase boundary, measured at $\theta = 3° > \theta_c$ and $\theta = 0° < \theta_c$, respectively. As B_{c2} increases with a decrease in temperature, at constant **I**, **F** also increases at lower temperatures. At $\theta = 3°$ for which the order parameter is uniform, ΔB_{c2} shows a clear activation behaviour due to the increase in **F** at lower temperatures. When $\theta = 0°$, ΔB_{c2} coincides with that measured at $\theta = 3°$ for $T > T^*$. Comparing the data in Fig. 2d,e, the deviation in ΔB_{c2} becomes visible for $T \leq T^*$ because of the pinning effect. These contrasting behaviours confirm T^* as the critical temperature to enter the orbital FFLO state.

The abrupt vortex pinning below θ_c at $T < T^*$ is consistent with the alternating phase vector **q** formed in the FFLO order parameter, switching polarities within a single unit cell (Fig. 2e). This phase configuration is analogous to the ground state of a Josephson π junction in which the net tunnelling of a supercurrent through the junction is zero. Effectively, the FFLO order parameter prohibits vortex motion driven by **F** in the out-of-plane direction[36]. As a result, on entering the FFLO phase below T^*, we observe that the pinning effect increases as T decreases (Fig. 2e).

Rotational symmetry breaking in an orbital FFLO state

The orbital FFLO state also breaks rotational symmetry in the basal plane—another hallmark signature to be measured by electrical transport[30]. In this work, the anisotropy manifests itself in the azimuthal angular dependence of the magnetoresistance $R(\varphi)$. To resolve this anisotropy, which is later identified as only approximately 1% of the

orbital FFLO state. The kinks observed in the $J_c(B)$ dependencies (**a**) determine the boundary of the first-order phase transition from the uniform Ising superconductivity to the orbital FFLO states (blue dots). The Ising superconductivity is isotropic with a two-fold symmetry caused by the Lorentz-force-induced vortex motion. The orbital FFLO phase exhibits an intrinsic six-fold anisotropy. The error bars are smaller than the symbol size.

gap size, we must eliminate the effect of the canting angle γ (Methods). Figure 3c shows the azimuthal angle (φ) dependence of $R_\parallel$ in parallel magnetic fields along the phase boundary $(T, B_{c2,\parallel})$ after correcting for γ (Methods and Extended Data Fig. 3). As shown in Fig. 3d–i, the anisotropy of $R_\parallel$ for different phases across T^* shows a two-fold to six-fold transition. For 2D angular mapping above T^*, $R(\varphi, \theta)$ oscillates at 180° with two-fold anisotropy, exhibiting the maxima and minima for the **B $\perp$ I** and **B $\parallel$ I** configurations, respectively (Fig. 3d–f). This directional dependence in **I** is further characterized in Fig. 3j when **I** is rotated by approximately 90° using orthogonal pairs of electrodes. Rotating **I** by approximately 90° causes a shift in the two-fold anisotropy by approximately 95° with a small deviation of 5° caused by the electrodes (Extended Data Fig. 4). This substantial shift indicates that the two-fold anisotropy has an extrinsic origin. The Lorentz force **F** becomes zero for **B $\parallel$ I** and reaches a maximum for **B $\perp$ I**. The anisotropy of **F** affects the dissipative motion of vortices, causing two-fold anisotropy (Fig. 3d–f,j), which is consistent with the report on bulk crystals[24] but different from another report on ultrathin NbSe$_2$ (ref. 37).

As shown in Fig. 3g–i, the emergence of six-fold anisotropy coincides with T^* (Fig. 3h) for which $R(\varphi, \theta)$ reaches its minima when the B field is applied along the crystalline direction of NbSe$_2$ at $\varphi = -60°$, 0° and 60°. In contrast to the two-fold anisotropy due to **F**, which shifts as **I** is rotated, applying an orthogonal **I** causes no shift in the six-fold anisotropy (Fig. 3i,k), indicating its intrinsic origin. From the $R_\parallel(\varphi)$ variation (Fig. 3c), we quantify the anisotropy as 0.8% of the largest superconducting gap at the K/K' pockets of NbSe$_2$ (Supplementary Information section 3). We also confirm the universal existence of six-fold anisotropy in another comparable high-quality sample with intermediate thickness, showing an upturn in B_{c2} (Extended Data Fig. 5). By contrast, similar controlled measurements carried out on ionic-gated MoS$_2$ exhibit uniform superconductivity, consistent with the picture of monolayer Ising superconductivity without interlayer interaction (Supplementary Information section 4).

Phase diagram of the orbital FFLO state

To resolve the first-order phase boundary between the FFLO state and the normal Ising superconducting phase, we measure the critical current density J_c as a function of T and $B_\parallel$ (Fig. 4a). Taking the measurement at 2.5 K as an example, we find that as J_c decreases with $B_\parallel$, a clear upturn appears at $B_\parallel = 5.5$ T. The kink smoothes out when the temperature increases to 6 K. By contrast, these kinks are not observed

in the temperature dependence of J_c when $B_\parallel = 0$, which rules out the multigap scenario as the cause of the upturn (Methods). Similar to the abrupt increase in B_{c2} (Fig. 2b) observed at the phase boundary, entering the orbital FFLO phase at a fixed temperature from the uniform phase also lowers the free energy[31,38], enhancing J_c. Therefore, we determine the phase boundary as the B field at which the upturn in J_c occurs (Fig. 4b). The extrapolation from the measured phase boundary aligns well with the tri-critical point (Fig. 4b, yellow dot), which is differently determined from the phase boundary by the upturn in $B_{c2}(T)$ (Fig. 1h).

Figure 4b shows the entire phase diagram consisting of a normal metal, a uniform Ising superconductor and the six-fold orbital FFLO phase. Based on symmetry considerations for multilayer $NbSe_2$ under $B_\parallel$, the distinctive change from isotropic to six-fold basal-plane anisotropy (Fig. 3d–i) around the tri-critical points (T^*, B^*) can be described by the Ginzburg–Landau free energy (Methods). We found that the critical field B^*, separating the zero-momentum uniform phase and the orbital FFLO phase, is nearly temperature independent, as consistently shown in the phase diagram (Fig. 4b). At high fields above the tri-critical point, Cooper pairs in the lth layer acquire alternating finite momentum $(-1)^l \mathbf{q}$ for which $\mathbf{q} \propto \mathbf{B} \times \mathbf{z}$, to minimize the free energy. Owing to the constraints of crystal rotation symmetries, the non-zero momentum q couples anisotropically to the B field, manifesting itself in higher-order terms (Methods). For $B < B^*$ and $q = 0$, T_c is isotropic. When $B > B^*$ and $q \neq 0$, the anisotropic part of the critical temperature is $\Delta T_c \propto \cos(6\varphi)$. This six-fold anisotropy of T_c is precisely captured by measuring $R(\varphi)$ in the coexisting state (Fig. 3g–i).

Our work demonstrates the existence of an orbital FFLO phase within an interlayer-coupled Ising superconductor. Similar orbital FFLO phases are expected after this general mechanism in many other multilayer Ising superconductors.

Online content

1. Fulde, P. & Ferrell, R. A. Superconductivity in a strong spin-exchange field. *Phys. Rev.* **135**, A550–A563 (1964).
2. Larkin, A. I. & Ovchinnikov, Y. N. Nonuniform state of superconductors. *Sov. Phys. JETP* **47**, 1136–1146 (1964).
3. Barzykin, V. & Gor'kov, L. P. Inhomogeneous stripe phase revisited for surface superconductivity. *Phys. Rev. Lett.* **89**, 227002 (2002).
4. Zheng, Z. et al. FFLO superfluids in 2D spin-orbit coupled Fermi gases. *Sci. Rep.* **4**, 6535 (2014).
5. Sigrist, M. et al. Superconductors with staggered non-centrosymmetricity. *J. Phys. Soc. Jpn* **83**, 061014 (2014).
6. Liu, C.-X. Unconventional superconductivity in bilayer transition metal dichalcogenides. *Phys. Rev. Lett.* **118**, 087001 (2017).
7. Nakamura, Y. & Yanase, Y. Odd-parity superconductivity in bilayer transition metal dichalcogenides. *Phys. Rev. B* **96**, 054501 (2017).
8. Hu, L.-H., Liu, C.-X. & Zhang, F.-C. Topological Larkin-Ovchinnikov phase and Majorana zero mode chain in bilayer superconducting topological insulator films. *Commun. Phys.* **2**, 25 (2019).
9. Bauer, E. & Sigrist, M. *Non-Centrosymmetric Superconductors: Introduction and Overview* Vol. 847 (Springer Science & Business Media, 2012).
10. Lu, J. M. et al. Evidence for two-dimensional Ising superconductivity in gated MoS_2. *Science* **350**, 1353–1357 (2015).
11. Xi, X. et al. Ising pairing in superconducting $NbSe_2$ atomic layers. *Nat. Phys.* **12**, 139–143 (2016).
12. Aslamazov, L. G. Influence of impurities on the existence of an inhomogeneous state in a ferromagnetic superconductor. *Sov. Phys. JETP* **28**, 773–775 (1969).
13. Takada, S. Superconductivity in a molecular field. II: stability of Fulde-Ferrel phase. *Prog. Theor. Phys.* **43**, 27–38 (1970).
14. Gruenberg, L. W. & Gunther, L. Fulde-Ferrell effect in type-II superconductors. *Phys. Rev. Lett.* **16**, 996–998 (1966).
15. Shimahara, H. Fulde-Ferrell state in quasi-two-dimensional superconductors. *Phys. Rev. B* **50**, 12760–12765 (1994).
16. Yuan, N. F. Q. & Fu, L. Topological metals and finite-momentum superconductors. *Proc. Natl Acad. Sci. USA* **118**, e2019063118 (2021).
17. Kumagai, K. et al. Fulde-Ferrell-Larkin-Ovchinnikov state in a perpendicular field of quasi-two-dimensional $CeCoIn_5$. *Phys. Rev. Lett.* **97**, 227002 (2006).
18. Kumagai, K., Shishido, H., Shibauchi, T. & Matsuda, Y. Evolution of paramagnetic quasiparticle excitations emerged in the high-field superconducting phase of $CeCoIn_5$. *Phys. Rev. Lett.* **106**, 137004 (2011).
19. Lortz, R. et al. Calorimetric evidence for a Fulde-Ferrell-Larkin-Ovchinnikov superconducting state in the layered organic superconductor κ-(BEDT-TTF)$_2$Cu(NCS)$_2$. *Phys. Rev. Lett.* **99**, 187002 (2007).
20. Beyer, R., Bergk, B., Yasin, S., Schlueter, J. A. & Wosnitza, J. Angle-dependent evolution of the Fulde-Ferrell-Larkin-Ovchinnikov state in an organic superconductor. *Phys. Rev. Lett.* **109**, 027003 (2012).
21. Uji, S. et al. Vortex dynamics and the Fulde-Ferrell-Larkin-Ovchinnikov state in a magnetic-field-induced organic superconductor. *Phys. Rev. Lett.* **97**, 157001 (2006).
22. Devarakonda, A. et al. Signatures of bosonic Landau levels in a finite-momentum superconductor. *Nature* **599**, 51–56 (2021).
23. Kinjo, K. et al. Superconducting spin smecticity evidencing the Fulde-Ferrell-Larkin-Ovchinnikov state in Sr_2RuO_4. *Science* **376**, 397–400 (2022).
24. Yasuzuka, S. et al. Highly isotropic in-plane upper critical field in the anisotropic s-wave superconductor $2H$-$NbSe_2$. *J. Supercond. Nov. Magn.* **33**, 953–958 (2020).
25. Fletcher, J. D. et al. Penetration depth study of superconducting gap structure of $2H$–$NbSe_2$. *Phys. Rev. Lett.* **98**, 057003 (2007).
26. Foner, S. & McNiff, E. J. Upper critical fields of layered superconducting $NbSe_2$ at low temperature. *Phys. Lett. A* **45**, 429–430 (1973).
27. de la Barrera, S. C. et al. Tuning Ising superconductivity with layer and spin–orbit coupling in two-dimensional transition-metal dichalcogenides. *Nat. Commun.* **9**, 1427 (2018).
28. Prober, D. E., Schwall, R. E. & Beasley, M. R. Upper critical fields and reduced dimensionality of the superconducting layered compounds. *Phys. Rev. B* **21**, 2717–2733 (1980).
29. Bulaevskii, L., Buzdin, A. & Maley, M. Intrinsic pinning of vortices as a direct probe of the nonuniform Larkin-Ovchinnikov-Fulde-Ferrell state in layered superconductors. *Phys. Rev. Lett.* **90**, 067003 (2003).
30. Croitoru, M. & Buzdin, A. In search of unambiguous evidence of the Fulde–Ferrell–Larkin–Ovchinnikov state in quasi-low dimensional superconductors. *Condens. Matter* **2**, 30 (2017).
31. Buzdin, A., Matsuda, Y. & Shibauchi, T. FFLO state in thin superconducting films. *Europhys. Lett.* **80**, 67004 (2007).
32. Denisov, D., Buzdin, A. & Shimahara, H. Types of Fulde-Ferrell-Larkin-Ovchinnikov states induced by anisotropy effects. *Phys. Rev. B* **79**, 064506 (2009).
33. Bulaevskiĭ, L. Inhomogeneous state and the anisotropy of the upper critical field in layered superconductors with Josephson layer interaction. *Sov. Phys. JETP* **38**, 634–639 (1974).
34. Devarakonda, A. et al. Clean 2D superconductivity in a bulk van der Waals superlattice. *Science* **370**, 231–236 (2020).
35. Kwok, W. et al. Direct observation of dissipative flux motion and pinning by twin boundaries in $YBa_2Cu_3O_{7-\delta}$ single crystals. *Phys. Rev. Lett.* **64**, 966–969 (1990).
36. Goldobin, E., Koelle, D., Kleiner, R. & Buzdin, A. Josephson junctions with second harmonic in the current-phase relation: properties of φ junctions. *Phys. Rev. B* **76**, 224523 (2007).
37. Hamill, A. et al. Two-fold symmetric superconductivity in few-layer $NbSe_2$. *Nat. Phys.* **17**, 949–954 (2021).
38. Doh, H., Song, M. & Kee, H. Novel route to a finite center-of-mass momentum pairing state for superconductors: a current-driven Fulde-Ferrell-Larkin-Ovchinnikov state. *Phys. Rev. Lett.* **97**, 257001 (2006).

Article

Methods

Device fabrication and measurement

We mechanically exfoliate $NbSe_2$ thin flakes from a bulk single crystal. The devices were made on a silicon substrate with an approximately 285-nm-thick oxide layer. Hexagonal boron nitride flakes were first exfoliated onto a polydimethylsiloxane substrate and dropped onto the $NbSe_2$ flake as the capping layer at room temperature. Both exfoliation and transfer processes were performed in an inert Ar atmosphere to prevent possible sample degradation. The electrodes (50 nm Au on 1 nm Ti) were deposited by electron-beam evaporation after etching through the hexagonal boron nitride capping layer in CF_4 plasma. The thicknesses of the $NbSe_2$ flakes were determined by atomic force microscopy. The devices were mounted on a two-axis rotating stage (atto3DR). The angles were determined by potential meters, which have an accuracy better than 0.1°. Three SR830 DSP lock-in amplifiers measured the electrical transport. Two Keithley meters, a 2450 source measurement unit and a 182 voltmeter, were used for the d.c. current–voltage measurements. If not specified, the data were measured on a 17-nm-thick flake with a constant current density of 0.003 MA cm^{-2}.

Nullifying the canting angles due to device installations

For a 2D superconductor, the angular dependence of the upper critical field $B_{c2}(\theta)$ is described by the 2D Tinkham formula[39]:

$$\frac{B_{c2}(\theta)\sin\theta}{B_{c2,\perp}} + \left(\frac{B_{c2}(\theta)\cos\theta}{B_{c2,\parallel}}\right)^2 = 1. \qquad (1)$$

Here θ is the angle between the B field and 2D plane; and $B_{c2,\perp}$ and $B_{c2,\parallel}$ are the upper critical fields when the field is perpendicular and parallel to the 2D plane, respectively.

For superconductors with strong anisotropy, such as in our orbital FFLO system, even a tiny canting from the precise in-plane alignment can substantially decrease B_{c2} because of the large $B_{c2,\parallel}/B_{c2,\perp}$ ratio. It is worth emphasizing that even if we can tune the instrumental alignment almost perfectly, each device installation onto the measurement system can inevitably cause misalignment. In reality, there always exists a canting angle γ, contributed by both instrumental and installation misalignment.

In our angular measurements, this unavoidable γ is eliminated by two-axis rotational mapping. As shown in Extended Data Fig. 2, we mount a 2D superconductor (yellow 2D plane) on a rotating stage (grey plane) with rotation axes 1 and 2. During sample installation, a canting angle γ is introduced between the sample and rotation plane. The γ value can be cancelled out by rotating axis 1 to align the sample plane with the B fields. Nevertheless, once the 2D sample is parallel to the field ($\theta = 0$), rotating axis 2 will again induce an angle between the sample plane and B field ($\theta \neq 0$) (Extended Data Fig. 2), which varies as

$$\theta(\varphi, \theta_0) = \arctan[\tan\gamma\cos(\varphi + \Phi_2)] - (\theta_0 + \Phi_1), \qquad (2)$$

with Φ_1 and Φ_2 being the phases of the readings from axes 1 and 2, respectively. The γ, Φ_1 and Φ_1 values become constants after the device installation. During the measurement, to keep the B field parallel to the crystal plane at different φ, one must continuously tune θ_0. As a result, the canting angle γ can be subtracted from the mapping of $R(\varphi, \theta_0)$ (Extended Data Fig. 3). The misalignment of the B field can shift the tri-critical point T^* to higher fields above the Pauli limit, which might have hindered the identification of the orbital FFLO[40].

Ginzburg–Landau model for the six-fold orbital FFLO state

To understand the origin of the six-fold anisotropy under an in-plane B field, we propose the following Ginzburg–Landau free energy of a multilayer $NbSe_2$ in the presence of an in-plane magnetic field $\mathbf{B}$ based on symmetries:

$$F = \sum_l \int d^2\mathbf{r} \left\{ \psi_l^* \alpha[(-)^l \mathbf{q}, \mathbf{B}] \psi_l - J(\psi_l^* \psi_{l+1} + \text{c.c.}) + \frac{1}{2}\beta |\psi_l|^4 \right\}, \qquad (3)$$

where $\psi_l(\mathbf{r}) = \int \frac{d^2\mathbf{q}}{(2\pi)^2} \psi_{l\mathbf{q}} e^{i\mathbf{q}\bullet\mathbf{r}}$ is the superconducting order parameter of layer $l = 1, 2\ldots$ in real space, $\mathbf{q} = -i\nabla$ is the in-plane momentum operator, $J > 0$ is the Josephson coupling and $\beta > 0$ is the quartic coefficient of the order parameter.

The second-order coefficient α is a function of momentum $\mathbf{q}$ and magnetic field $\mathbf{B}$, and the layer-dependent alternating sign $(-)^l$ is due to the global inversion symmetry:

$$I: \mathbf{q} \to -\mathbf{q}, \ \mathbf{B} \to \mathbf{B}, \ \psi_l \to \psi_{N+1-l'}$$

where N is the total number of layers. Together with the time-reversal symmetry, in-plane mirror symmetry and in-plane rotation symmetry, we can determine the general form of α as

$$\alpha(\mathbf{q}, \mathbf{B}) = a(T - T_0) + b\mathbf{q}\bullet(\mathbf{B} \times \mathbf{z}) + cq^2 + dB^2 + \lambda_1 \text{Re}(q_+^2 B_+^4) + \lambda_2 \text{Re}(q_+^4 B_+^2) + \ldots, \qquad (4)$$

where $a, c > 0$ for stability, $q_+ = q_x + iq_y$ and $B_+ = B_x + iB_y$. The parameters a, b, c, d and $\lambda_{1,2}$ are determined by microscopic details of the system, such as the density of states, Fermi velocity, SOC, Fermi surface anisotropy and interlayer coupling. The dimensionless quantity $Jc/(bB)^2$ controls the phase transition in equation (4).

It is demanding to analytically solve the complete problem with N layers. Therefore, without losing the essential physics, we examine the most straightforward multilayer system containing $N = 2$, forming the Bloch configuration. For this bilayer case, equation (4) can be perturbatively solved by treating $\lambda_{1,2}$ as perturbations. For general N layers, the order parameter can be obtained from the bilayer states, as discussed below.

When $\lambda_{1,2} = 0$, by minimizing the free energy, we can find two kinds of superconducting phase near the superconducting–normal phase transition. The different Cooper-pair momentum $\mathbf{q}$ characterizes these two phases and hence different upper critical fields, or equivalently, the B-field dependence of the critical temperature T_c.

For $B < B^*$,

$$q = 0, \ T_c = T_0 + J/a - dB^2/a.$$

For $B \geq B^*$,

$$\mathbf{q}_l = (-)^l \frac{b}{2c}(\mathbf{B} \times \mathbf{z})\sqrt{1 - \left(\frac{B^*}{B}\right)^4}, \ T_c = T_0 + \frac{b^2}{4ac}\left(B^2 + \frac{|B^*|^4}{B^2}\right) - \frac{d}{a}B^2.$$

The tri-critical point (T^*, B^*) is

$$B^* = \frac{\sqrt{2Jc}}{b}, \ T^* = T_0 + J/a - d|B^*|^2/a.$$

The location of the tri-critical point (T^*, B^*) is mainly determined by the interlayer Josephson coupling J. When the interlayer Josephson coupling is turned off, that is, let $J = 0$, we find $T^* = T_{c0}$. This means that at any finite field, each layer has Cooper pairs with alternating finite momentum $(-)^l\mathbf{q}$, which is consistent with our previous argument. Also, we can determine the numerical constant relating B^* and $\sqrt{Jc}/b$, consistent with our dimensional analysis discussed in the main text.

Next, we turn on the weak anisotropy by letting $\lambda_{1,2} \neq 0$, which are the perturbations. All these anisotropic terms are $\mathbf{q}$ dependent and vanish at zero momentum; hence, we find that the BCS phase at $q = 0$ is always

isotropic. By contrast, the orbital FFLO phase with finite Cooper-pair momentum shows six-fold anisotropy under an in-plane B field.

For $B < B^*$,

$$q = 0,\ T_c = T_0 + J/a - dB^2/a.$$

However, for $B > B^*$,

$$\mathbf{q}_l = (-)^l \frac{b}{2c}(\mathbf{B} \times \mathbf{z})\sqrt{1 - \left(\frac{B^*}{B}\right)^4},$$

$$T_c = T_0 + \frac{b^2}{4ac}\left(B^2 + \frac{|B^*|^4}{B^2}\right) - \frac{d}{a}B^2 + \lambda(B)\cos(6\varphi),$$

where $\lambda(B)$ depends only on the magnitude of the field, and $\varphi = a\tan(B_y/B_x)$ is the polar angle denoting the direction of the in-plane B field.

For the general case of an N-layer system, we expect the order parameter to form a Bloch-like configuration based on the bilayer states above, having the two-component order parameter as

$$\Psi_l = \begin{pmatrix} \psi_{2l-1} \\ \psi_{2l} \end{pmatrix}.$$

Then, we obtain the free energy of the multilayers as

$$F = \sum_l \int d^2\mathbf{r}\left\{\Psi_l^\dagger A\Psi_l - J(\Psi_l^\dagger \sigma_-\Psi_{l+1} + \text{h.c.}) + \frac{1}{2}\beta\,|\Psi_l^\dagger\Psi_l|^2\right\}, \qquad (8)$$

$$A = \begin{pmatrix} \alpha_- & -J \\ -J & \alpha_+ \end{pmatrix}, \sigma_- = \begin{pmatrix} 0 & 0 \\ 1 & 0 \end{pmatrix}, \alpha_\pm = a(T - T_0) \pm b\mathbf{q}\cdot(\mathbf{B}\times\mathbf{z}) + cq^2 + \dots.$$

As the free energy above has the translation symmetry $\Psi_l \to \Psi_{l+1}$, according to the Bloch theorem, we expect our solution to satisfy $\Psi_{l+1} = e^{i\theta}\Psi_l$, or equivalently,

$$\Psi_l = e^{il\theta}\Psi_0.$$

Here $\theta \in (-\pi, \pi]$ is the Bloch-phase modulation parameter to be determined soon. With this ansatz of the order parameter, the free energy above becomes

$$F = \sum_l \int d^2\mathbf{r}\left\{\Psi_0^\dagger A\Psi_0 - 2J\Psi_0^\dagger(\sigma_+ e^{i\theta} + \sigma_- e^{i\theta})\Psi_0\cos\theta + \frac{1}{2}\beta\,|\Psi_0^\dagger\Psi_0|^2\right\}, \sigma_+ = \sigma_-^\dagger. \qquad (9)$$

When minimizing the free energy, we obtain $\theta = 0$. In other words, $\Psi_l = \Psi_0$ and every bilayer shares the same order-parameter configuration. Therefore, the superconducting phases worked out from the bilayer NbSe$_2$ model can be extended to the multilayers.

Excluding other possible scenarios for the upturn in $B_{c2}(T)$

The upturn in $B_{c2}(T)$ is associated with out-of-plane translational and in-plane rotational symmetries breaking, which is consistent with the orbital FFLO model. Several other scenarios can also support the upturn in $B_{c2}(T)$, such as intrinsic two-gap superconductivity, the Takahashi–Tachiki effect, spin-triplet pairing and three-dimensional (3D)–2D crossover. In this section, these scenarios are discussed and eventually ruled out.

Two-gap superconductivity

The superconducting gaps of NbSe$_2$ open at both K and Γ points for both hole- and electron-like pockets, as shown in the angle-resolved photoemission spectroscopy results[41,42]. The superconductivity of the Se-derived (Fig. 1f, grey circle) Γ pocket has a tiny gap[43] or is gapless[41,42]. The multiple gaps of different gap sizes may lead to kinks in both

$B_{c2}(T)$ (ref. 44) and $J_c(T)$ (ref. 45). On the other hand, in dirty two-gap superconductors, the upturn in $B_{c2}(T)$ is also expected due to interband scattering[44].

First, we can rule out the possibility of having the dirty two-gap scenario as our device shows superconductivity in the clean regime. Furthermore, the kink observed in $|\theta| < 1°$ ($B_{c2}(\theta)$; Fig. 2b) cannot be described by the dirty two-gap model[44]. Second, within the two-gap scenario, one would expect the temperature dependence of J_c to show a kink when the second gap opens at $T < T_{c0}$ under the zero B field[45]. As shown in Extended Data Fig. 7, the $J_c(T)$ value measured at $B = 0$ T has a smooth dependence without showing a kink as a function of temperature. Instead, the kinks in J_c appear when the B field is applied crossing the uniform superconductor–orbital FFLO phase boundary (Fig. 4a). The phase boundary thus determined by $J_c(B)$ agrees well with the tri-critical point that is determined by $B_{c2}(T)$ measurements. Hence, we can also safely rule out the two-gap scenario as the cause of the kinks observed in our devices.

Takahashi–Tachiki effect

The Takahashi–Tachiki effect describes a superconducting superlattice consisting of stacked superconducting bilayers. Two types of superconductor in the bilayers, the N and S layers, have the same T_{c0} but different diffusion constants[46]. Both N and S superconductors are in the dirty limit. Therefore, the large and small diffusion constants (denoted as D_N and D_S, respectively) lead to low and high B_{c2} values, respectively. A new superconducting phase appears—when the D_N/D_S ratio exceeds a critical value—as an upturn in the temperature dependence of B_{c2}. The B_{c2} upturn is associated with the preferential nucleation of superconductivity in one of the two layers. Order parameters beyond the upturn are concentrated in the S layers with higher B_{c2} and hence are more robust at higher fields. As the physical picture of the Takahashi–Tachiki effect is fundamentally different from our orbital FFLO state, they apply to very different regimes.

First, the Takahashi–Tachiki effect is explicitly developed for dirty superconductors, when both types of superconductor are in the dirty limit for which the competition and selective nucleation depend on D_S and D_N. By contrast, our sample is in the clean regime (Supplementary Information section 1), which is consistent with the high RRR value (Fig. 1g). Furthermore, our system's large Ising SOC pins the spin in the out-of-plane direction, protecting the electron spins from being scattered by impurities. Therefore, the assumption of a dirty regime used in the Takahashi–Tachiki model for which scattering determines the diffusion length[46] may not apply to our system.

According to the Takahashi–Tachiki model, $B_{c2,S}/B_{c2,N} = 15$ merely brings the upturn to $T^* \approx 0.5T_{c0}$ (ref. 46). To achieve $T^* = 0.84T_{c0}$ (Fig. 4), an unrealistically large $B_{c2,N}/B_{c2,S}$ is required. In NbSe$_2$, the highest in-plane B_{c2} reported so far is almost $7B_P$ for which the lowest B_{c2} is found in pristine bulk for almost $1B_P$. Therefore, the largest B_{c2} ratio accessible in the NbSe$_2$ systems only reaches 7, which is less than half of $B_{c2,S}/B_{c2,N} = 15$. As the $B_{c2,S}/B_{c2,N}$ ratio increases, increasingly sharper upturns are expected. By contrast, experimentally, we observed a smooth upturn in $B_{c2}(T)$. In short, the relatively soft upturn and high T^* observed in our uniform single-crystal sample cannot be reconciled with the Takahashi–Tachiki theory. It is worth noting that the Takahashi–Tachiki model has one more characteristic temperature close to T_{c0}, corresponding to a 2D–3D crossover[46]. By contrast, our 17-nm flake (Fig. 1h) shows no linear $B_{c2}(T)$ dependence, which is inconsistent with the Takahashi–Tachiki theory.

The first-order transition described by the Takahashi–Tachiki effect involves a competition between the coherence length ξ and the magnetic length $l_B = 1/\sqrt{2eB}$, which vary with temperature and B field, respectively. Such competition leads to a first-order phase transition relying on both temperature and field, which appears as a diagonal in the phase diagram[46]. In our orbital FFLO picture, this first-order phase transition line is expected to have a weak temperature dependence.

Article

As shown in equation (4), the transition from uniform to orbital FFLO state is determined by $Jc/(bB)^2$ for which a weak temperature dependence is expected for J. Indeed, experimentally, the first-order phase transition line weakly depends on temperature (Fig. 4b), which is inconsistent with the Takahashi–Tachiki model.

Spin-triplet pairing

Due to the non-centrosymmetric crystal structure of monolayer transition metal dichalcogenides, the spin splitting induced by Ising SOC may lead to mixed singlet and triplet pairing[47], which also enhances B_{c2} (ref. 48). Experimentally, the B_{c2} value of spin-triplet superconductivity characterizes a non-saturating temperature dependence due to the diverging paramagnetic limit. The non-saturating B_{c2} value has been reported in bulk spin-triplet superconductor UTe$_2$, violating the limits set by the orbital depairing effect and Pauli paramagnetism[49]. In transition metal dichalcogenides, the spin-triplet superconductivity was not experimentally observed in monolayer MoS$_2$ (refs. 10,50) or in NbSe$_2$ (ref. 27). In our work, B_{c2} increases moderately and saturates at low temperatures, which is inconsistent with the spin-triplet scenario. Furthermore, the spin-triplet pairing cannot explain the vortex pinning (Fig. 2). Therefore, we can rule out spin-triplet pairing as the candidate mechanism.

Dimensional crossover from three dimensions to two dimensions

An upturn in B_{c2} has been widely observed in layered superconductors as a 3D–2D crossover. Close to T_c, the B_{c2} value is described by the 3D Ginzburg–Landau model. Similar to the Takahashi–Tachiki model, the phenomenological model valid in the scale of the coherence length relies on the temperature dependence of the coherence length. The fingerprint of such a crossover is a linear B_{c2} dependence on temperature near T_{c0}. The upturn due to dimensional crossover is well described by the Klemm–Luther–Beasley model[51]. For double-side gated bilayer MoS$_2$, a dimensional-crossover-related upturn is present due to interlayer Josephson coupling[52].

In our data, the 3D–2D crossover scenario seems to capture the upturns of B_{c2} in our 34- and 39-nm-thick samples, which have linear B_{c2} dependencies on temperature (Fig. 1i). However, in 12–22 nm NbSe$_2$, the B_{c2} value shows a square-root temperature dependence after the 2D Ginzburg–Landau model, suggesting 2D superconductivity at higher temperatures close to T_{c0}. As the 3D state is unavailable in the first place, the 3D–2D crossover cannot exist.

Furthermore, in our 17-nm flake, the 2D nature of superconductivity is confirmed (Fig. 2a,b), featuring a cusp-shaped 2D angular dependence of B_{c2} for the whole temperature range below T_{c0}. Therefore, the 3D–2D crossover cannot describe the observed B_{c2} upturn.

Excluding nodal superconductivity and intrinsic gap anisotropy scenario for six-fold anisotropy

When the magnetic field is applied along the Γ–M lines at which the Ising SOC vanishes, the Zeeman effect can align the spins to the in-plane direction, and thus, the gap is closed. The Cooper pairing away from the Γ–M lines is still protected by Ising SOC and leads to a finite superconducting gap. Therefore, the nodal superconducting phase is suggested to exist above the Pauli limit[53], and exhibits six-fold anisotropy[54]. Recent work in monolayer NbSe$_2$ (ref. 55) reported six-fold anisotropy in parallel magnetic fields at $T = 0.9T_{c0}$, which transforms into two-fold anisotropy at $T = 0.5T_{c0}$. The six-fold anisotropy is suggested to be nodal superconductivity when the B field is applied along the Γ–M lines, whereas the two-fold anisotropy is interpreted as nematic superconductivity.

Our results on multilayer NbSe$_2$ are very different compared with theoretical[53] and experimental reports[55]. First, the six-fold superconducting phase appears well below the Pauli limit, which is not consistent with the theoretical prediction of nodal superconductivity[53]. As the uniform–orbital FFLO phase boundary is determined by Josephson coupling, the boundary can be well below the Pauli limit[6].

On the other hand, the anisotropy transition in monolayer NbSe$_2$ (ref. 55) is essentially different from our results. In the monolayer case, the anisotropy transition is driven by temperature. The six-fold nodal superconductivity is observed at $T = 0.9T_{c0}$, and the two-fold nematic phase is observed at $T = 0.5T_{c0}$. By contrast, the anisotropy transition in the orbital FFLO state is driven by magnetic fields. As indicated in Fig. 4b, the normal–orbital FFLO phase boundary has a weak temperature dependence. Furthermore, the two-fold anisotropy is extrinsically induced by the Lorentz force. Therefore, the anisotropy transition is from isotropic to six-fold in our work, which is different from the report of nodal superconductivity[55]. With the above discussion, the scenario of nodal superconductivity can be ruled out in our work.

The intrinsic superconducting gap anisotropy of NbSe$_2$ has six-fold symmetry, as shown by angle-resolved photoemission spectroscopy and scanning tunnelling microscopy measurements[41,42]. Nevertheless, our observation is a symmetry transition close to T^* and B^*. Therefore, for $B < B^*$ for which the intrinsic gap anisotropy is intact, we can resolve only the extrinsic two-fold symmetry due to the Lorentz force, excluding the intrinsic gap anisotropy as the origin of the six-fold symmetry found for $B > B^*$.

Possible phase transition at lower temperatures

We noticed that pair density wave (PDW) superconductivity, which competes with the orbital FFLO phase, is an alternative candidate at lower temperatures and higher magnetic fields[7]. If it exists, one can expect another upturn in $B_{c2}(T)$ at low temperatures at which the transition from orbital FFLO to the PDW phase occurs. Meanwhile, after the theoretical prediction for conventional FFLO, a complex orbital FFLO state with multiple **q** phases may be energetically favoured at low temperatures[56–58]. However, the present measurement shows that $B_{c2}(T)$ smoothly saturates at $T = 0.35$ K (Fig. 1h) without any additional signature of PDW or multiple **q** phases. Our result, however, does not rule out the possibility that the PDW and multiple-**q** orbital FFLO states may exist at an even lower temperature for which alternative configurations of broken translational symmetry may also be valid.

Data availability

All relevant data shown are provided with this paper. Additional data that support the plots and other analyses in this work are available from the corresponding author upon request.

39. Harper, F. E. & Tinkham, M. The mixed state in superconducting thin films. *Phys. Rev.* **172**, 441–450 (1968).
40. Cho, C. et al. Evidence for the Fulde–Ferrell–Larkin–Ovchinnikov state in bulk NbS$_2$. *Nat. Commun.* **12**, 3676 (2021).
41. Rahn, D. J. et al. Gaps and kinks in the electronic structure of the superconductor 2H-NbSe$_2$ from angle-resolved photoemission at 1K. *Phys. Rev. B* **85**, 224532 (2012).
42. Kiss, T. et al. Charge-order-maximized momentum-dependent superconductivity. *Nat. Phys.* **3**, 720–725 (2007).
43. Dvir, T. et al. Spectroscopy of bulk and few-layer superconducting NbSe$_2$ with van der Waals tunnel junctions. *Nat. Commun.* **9**, 598 (2018).
44. Gurevich, A. Enhancement of the upper critical field by nonmagnetic impurities in dirty two-gap superconductors. *Phys. Rev. B* **67**, 184515 (2003).
45. Talantsev, E. F. et al. On the origin of critical temperature enhancement in atomically thin superconductors. *2D Mater.* **4**, 025072 (2017).
46. Takahashi, S. & Tachiki, M. New phase diagram in superconducting superlattices. *Phys. Rev. B* **34**, 3162–3164 (1986).
47. Gor'kov, L. P. & Rashba, E. I. Superconducting 2D system with lifted spin degeneracy: mixed singlet-triplet state. *Phys. Rev. Lett.* **87**, 037004 (2001).
48. Frigeri, P. A., Agterberg, D. F., Koga, A. & Sigrist, M. Superconductivity without inversion symmetry: MnSi versus CePt$_3$Si. *Phys. Rev. Lett.* **92**, 097001 (2004).
49. Ran, S. et al. Nearly ferromagnetic spin-triplet superconductivity. *Science* **365**, 684–687 (2019).
50. Saito, Y. et al. Superconductivity protected by spin–valley locking in ion-gated MoS$_2$. *Nat. Phys.* **12**, 144–149 (2016).
51. Klemm, R. A., Luther, A. & Beasley, M. R. Theory of the upper critical field in layered superconductors. *Phys. Rev. B* **12**, 877–891 (1975).
52. Zheliuk, O. et al. Josephson coupled Ising pairing induced in suspended MoS$_2$ bilayers by double-side ionic gating. *Nat. Nanotechnol.* **14**, 1123–1128 (2019).

53. He, W. Y. et al. Magnetic field driven nodal topological superconductivity in monolayer transition metal dichalcogenides. *Commun. Phys.* **1**, 40 (2018).

54. Shaffer, D., Kang, J., Burnell, F. J. & Fernandes, R. M. Crystalline nodal topological superconductivity and Bogolyubov Fermi surfaces in monolayer NbSe$_2$. *Phys. Rev. B* **101**, 224503 (2020).

55. Cho, C. et al. Nodal and nematic superconducting phases in NbSe$_2$ monolayers from competing superconducting channels. *Phys. Rev. Lett.* **129**, 087002 (2022).

56. Shimahara, H. Structure of the Fulde-Ferrell-Larkin-Ovchinnikov state in two-dimensional superconductors. *J. Phys. Soc. Jpn* **67**, 736–739 (1998).

57. Bowers, J. A. & Rajagopal, K. Crystallography of color superconductivity. *Phys. Rev. D* **66**, 065002 (2002).

58. Matsuda, Y. & Shimahara, H. Fulde–Ferrell–Larkin–Ovchinnikov state in heavy fermion superconductors. *J. Phys. Soc. Jpn* **76**, 051005 (2007).

59. Maloney, M. D., de la Cruz, F. & Cardona, M. Superconducting parameters and size effects of aluminum films and foils. *Phys. Rev. B* **5**, 3558–3572 (1972).

60. Kozuka, Y. et al. Two-dimensional normal-state quantum oscillations in a superconducting heterostructure. *Nature* **462**, 487–490 (2009).

61. Wang, B. Y. et al. Isotropic Pauli-limited superconductivity in the infinite-layer nickelate Nd$_{0.775}$Sr$_{0.225}$NiO$_2$. *Nat. Phys.* **17**, 473–477 (2021).

62. Takada, S. & Izuyama, T. Superconductivity in a molecular field. I. *Prog. Theor. Phys.* **41**, 635–663 (1969).

Author contributions P.W., O.Z. and J.Y. conceived the research. P.W., O.Z., X.P., L.Z. and M.L. fabricated the devices. P.W. carried out the magnetotransport and anisotropy measurements. P.W., O.Z., X.P., S.W. and U.Z. carried out the high-field magnetotransport measurements. N.F.Q.Y. constructed the theoretical model of the orbital FFLO states. P.W. and J.Y. analysed the data. P.W., N.F.Q.Y. and J.Y. interpreted the data and prepared the manuscript with inputs from N.E.H. and T.T.M.P. All authors commented on the manuscript.

Article
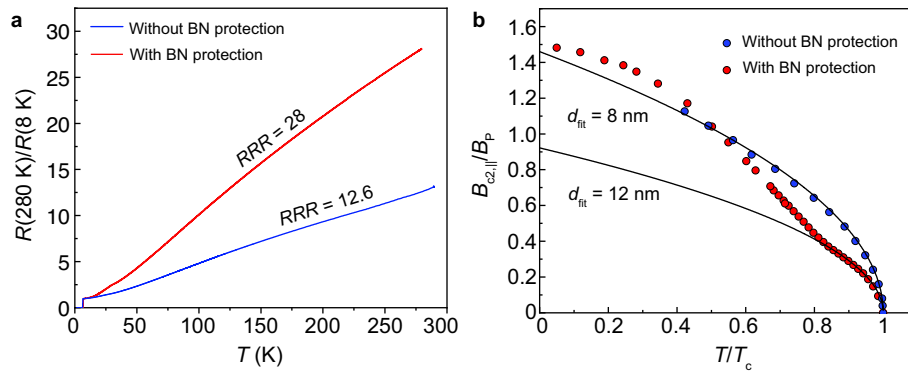
Extended Data Fig. 1 | Absence of the upturn in upper critical fields in a downgraded device. a, The temperature dependence of sheet resistances for two flakes showing RRR = 12.6 and 28 for 11 and 17 nm thick flakes, respectively. **b**, The $B_{c2,\parallel}$ measured for the 11 and 17 nm thick flakes. The 2D Ginzburg-Landau fittings, that is, the solid black curves, yield thickness d_{fit} = 8 and 12 nm, respectively. Overall, the reduced thicknesses obtained from the GL fittings are due to the protection from the Ising SOC, which becomes more robust in thinner flakes[59–61]. Close to T_{c0}, the 11 nm flake shows a steeper temperature dependence of B_{c2}, consistent with its reduced thickness. Nevertheless, for the 17 nm flake with a larger RRR, an upturn in the B_{c2} can be observed at $B = 0.36B_P$, indicating the orbital FFLO state, which eventually enhances B_{c2} to exceed that measured in the 11 nm flake. As a larger RRR indicates better sample quality, the contrasting behaviour in the temperature dependence of B_{c2} suggests that the absence of the orbital FFLO phase in the thin flake might be caused by the downgraded quality, which suppresses the finite-momentum pairing via scattering[13,62].
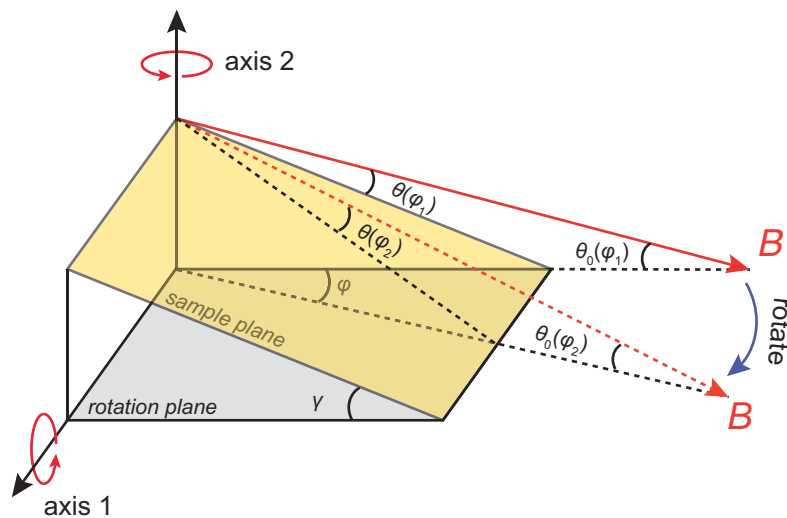
Extended Data Fig. 2 | Illustration of 2-axis rotation of a 2D sample in an external magnetic field with an installation canting angle γ. A 2D sample is mounted on a 2-axis rotational stage. The 2D surface of the sample (yellow plane) makes a canting angle γ with respect to one of the rotation planes of the stage (grey plane). To simplify the discussion and isolate the effect of canting angle γ, we assume that the stage can make precise rotations so that, as shown in Fig. 3b, we can always align the sample plane precisely parallel to the external B field. When this exact parallelism is aligned at a given φ, due to the canting angle γ, further rotation along the stage axis 1 or 2 can cause a correlation between θ and φ, which are labelled as different $\theta(\varphi)$ values.
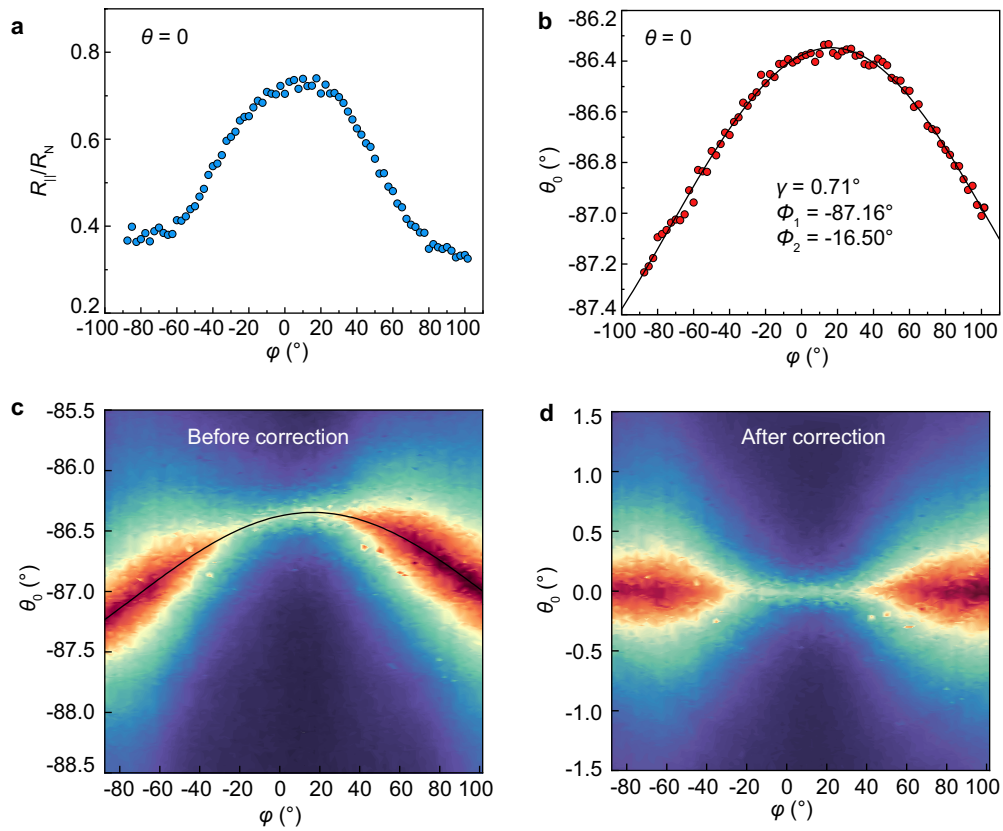
**Extended Data Fig. 3 | Procedure for subtracting the canting angle γ.**
a, Magnetoresistance $R_{\parallel}(\varphi)$ in an in-plane B field $B_{\parallel}$ (for the 17 nm device).
b, Variation of θ_0 (as defined in Extended Data Fig. 2) as a function of φ when the B field is adjusted to be parallel to the sample plane. The solid black curve is fitted using Eqn. 2 when $\theta = 0°$, which yields a canting angle $\gamma = 0.71°$. **c**, The data are shown in Fig. 2f before correcting the effect of γ. The black line is the same fitting that is shown in panel **b**. **d**, After correcting for the canting angle, the magnetoresistance $R(\varphi, \theta)$ shows a two-fold anisotropy.
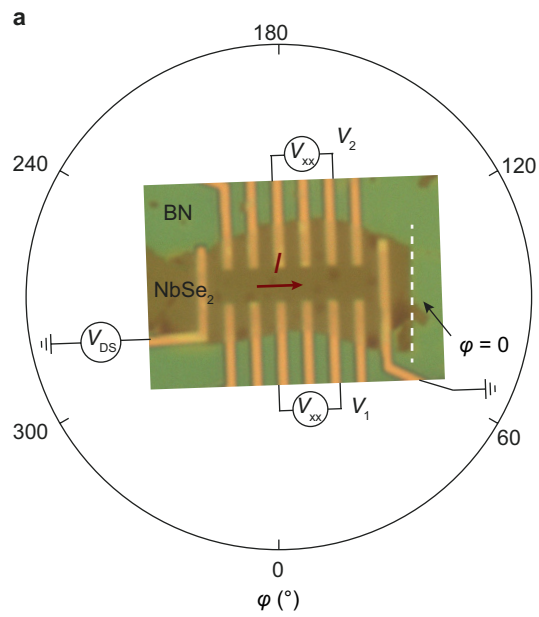
Extended Data Fig. 4 | Measurement configuration of the 17 nm device.
a, Device orientation and the applied current direction. One crystalline direction of NbSe$_2$, as indicated by the white dashed line, is defined as $\varphi = 0$.
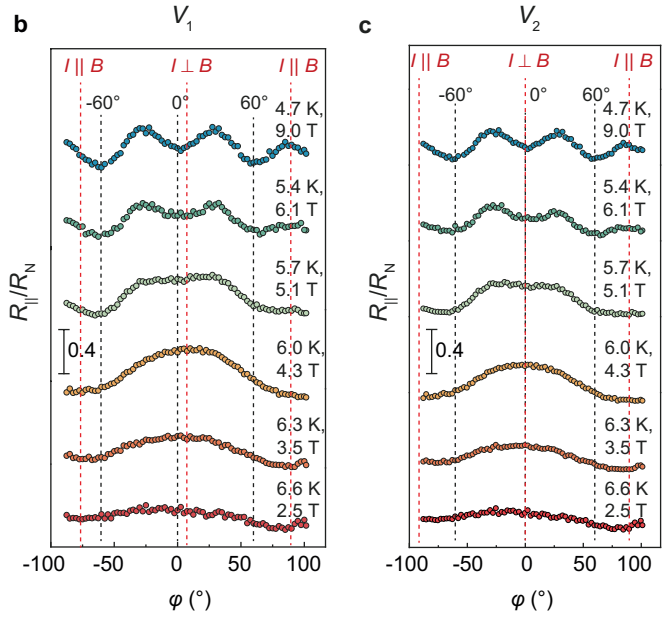
b, **c**, Transport measurements using two sets of electrode pairs on two sides of the Hall bar show a small shift (-5°). It is consistent with the small deviation of φ when changing the current direction in Fig. 3j.

a

b
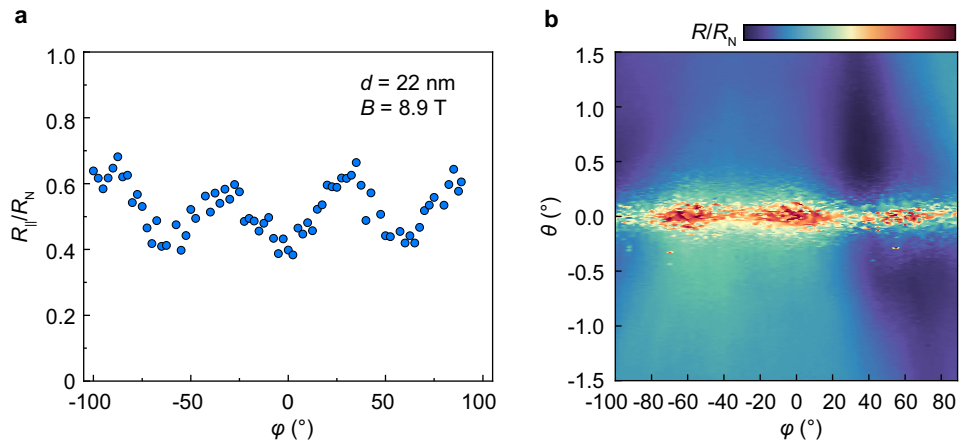
Extended Data Fig. 5 | Six-fold anisotropy of another multilayer NbSe$_2$ flake. The thickness of the flake is 22 nm. The anisotropy is measured at $B_\parallel$ = 8.9 T. **a**, The magnetoresistance $R_\parallel(\varphi)$ in the coexisting state shows a six-fold anisotropy in the $B_\parallel$ field. **b**, The mapping of $R(\theta, \varphi)$ exhibits six-fold anisotropy when rotating θ close to 0.
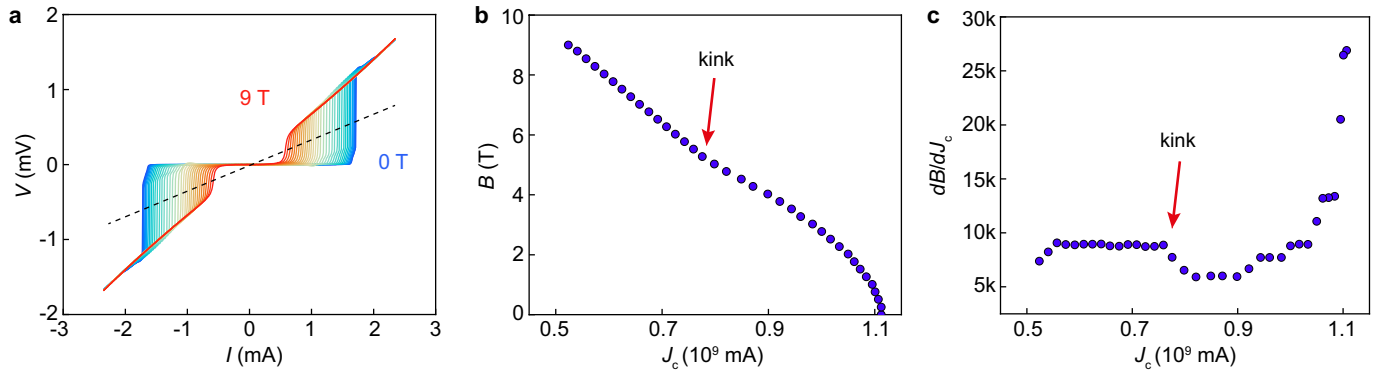
Extended Data Fig. 6 | Determination of the critical point where the upturn of $B_{c2}(J_c)$ occurs. a, An example of I-V measurements at different $B_\parallel$ fields at a fixed temperature. **b**, The critical current densities J_c were extracted from **a**. The critical current density is determined as the point where V/I is half the normal resistance R_N at $T = 10$ K. **c**, The upturn in the B–J_c plot is determined by the kink in dB/dJ_c.
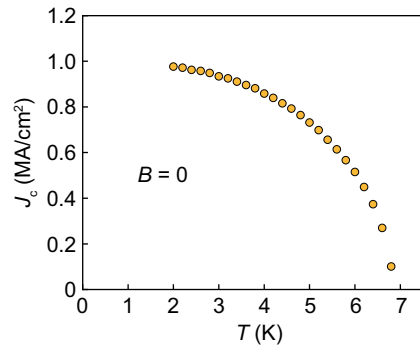
Extended Data Fig. 7 | Critical current density as a function of temperature under zero magnetic field. At $B = 0$ T, no upturn was observed in the temperature dependence of J_c, ruling out the two-gap scenario as the cause of the upturns.